ORIGINAL ARTICLE

Implications of pore space characteristics on diffusive transport in basalts and granites

Stefan Dultz · Anna V. Simonyan · Julio Pastrana ·
Harald Behrens · Michael Plötze · Thomas Rath

Abstract A detailed characterization of the pore space is crucial for understanding of transport and element transfer in rocks. Here, the effect of differences in texture and content of secondary minerals on transport in pore systems was determined for two rocks of widespread occurrence, mid-ocean ridge basalts (MORB) and granites. Pore space characteristics were analyzed by Hg-porosimetry, intrusion of a molten alloy, and synchrotron-based X-ray tomographic microscopy. For evaluating the role of pore space characteristics for the prediction of diffusive transport, data on porosity, and the effective diffusion coefficient (D_{eff}) were compared. Extended connective pore systems due to cracks and mineral dissolution are present in samples of both rocks, indicating high internal specific surface area. Uneven pore size distributions in altered MORB samples can be assigned to secondary minerals. Pore spaces determined by X-ray tomography, used to determine main direction of pores in the 3-D orthogonal system, suggest a slight anisotropy. In log–log plots, both rocks show roughly a linear dependence of D_{eff} for H_2O and compounds with comparable diffusivities (D_2O, monovalent cations, and anions) on porosity, but at same porosity D_{eff} is clearly higher in granitic than in basaltic samples. This difference is increasing with decreasing porosity, indicating that at low porosities the efficiency of element transport in basaltic samples is diminished, mainly inherited by the presence of small pores slowing down diffusion. The fact that diffusive transport in basaltic rocks is stronger dependent on porosity than in granitic rocks shows that also other rock characteristics such as pore size distribution and tortuosity of the pore network, highly affected by the alteration degree, can markedly affect transport and reactivity of pore solution.

Keywords Mid-ocean ridge basalt · Granite · Pore space characteristics · Wood's metal intrusion · X-ray-tomographic microscopy · Hg-porosimetry · Diffusive transport

S. Dultz (✉)
Institute of Soil Science, Leibniz University Hannover,
Herrenhäuser Str. 2, 30419 Hannover, Germany
e-mail: dultz@ifbk.uni-hannover.de

A. V. Simonyan · H. Behrens
Institute of Mineralogy, Leibniz University Hannover,
Callinstr. 3, 30167 Hannover, Germany

J. Pastrana · T. Rath
Institute for Biological Production Systems, Leibniz University
Hannover, Herrenhäuser Str. 2, 30419 Hannover, Germany

M. Plötze
Institute for Geotechnical Engineering, ETH Zürich,
8093 Zürich, Switzerland

Introduction

Chemical reactions at the mineral-water interface by both abiotic and biotic processes are of high importance for element transfer. Reactions are driven by the fact that minerals from magmatic or metamorphic origin are not stable under the respective solution chemistry and biological processes. Especially in cracks of rocks with fast moving water, conditions are far from equilibrium of the primary minerals. Mineral weathering is a decisive geochemical process for the quality of groundwater (Ganyaglo et al. 2011). The available specific surface area (SSA), which is related with the pore space and geometry is a decisive factor for the overall mineral dissolution rate (Lüttge 2005; Molina Ballesteros et al. 2011). Processes of

fluid flow and solute transport in the connected pore space are affected by the porosity, tortuosity, and pore size distribution. These parameters of the pore structure combine topological parameters such as pore connectivity and geometrical factors such as pore body and throat radius distributions (Dullien 1992; Hu et al. 2012).

Igneous rocks often have a poor primary permeability, but silicate weathering results in an increased secondary permeability. Initially, pores are related to final crystallization of melt relicts, thermal contraction during cooling and tectonic stresses, whereby the latter two issues induce intra- and intergranular cracks. Such macro- and micro-sized cracks can provide direct conduits for fluid transport, where bulk motion of solution is the transport mechanism. Commonly during dissolution–reprecipitation processes at hydrothermal alteration and weathering some material is lost to the fluid phase, increasing the porosity (Putnis 2002). Pore systems with relatively fine pores propagating from cracks along highly reactive sites in minerals are formed. Chemical weathering of minerals is strongly related with intergranular microtextures and microstructures (Lee et al. 1998), where preferential dissolution occurs at dislocations and defect structures, initiating the formation of extended tortuous pore systems. The rates of dissolution processes and the kind and quantity of secondary minerals formed highly depend on pore solution chemistry (Wilson 2004).

The portion of connected pores in relation to total porosity increases with increasing weathering degree. The contribution of such porous systems to actual weathering processes might be a rate-limiting step as transport is diffusion controlled (Cussler 1997). Therefore, a quantitative understanding of the effects of pore space characteristics on diffusive transport is needed which is a prerequisite for developing models for the description of the transport of solutes in rocks.

For the formation of the pore system, the susceptibility of the rock to weathering related with the structure, the presence of intergranular microtextures and chemical composition of minerals is a control. For studying the effect of different rock properties on the porosity and consequences for element turnover, here two different rocks are compared, basalt samples from mid-ocean ridge (MOR) systems and granite samples from soil and saprolite. During weathering basalt can loose almost all primary minerals, which are replaced to some extent by secondary minerals such as layer silicates and oxides whereas granite tends to maintain texture due to the presence of highly resistant quartz and alkali-feldspar and the much weaker tendency to form secondary minerals.

The rocks investigated in this study have strong significance for local and global element cycles. In hydrothermal MOR systems with a total length of 70,000 km high

volumes of water are cycled, emphasizing marked rock–water interactions. Strong heterogeneities in many ways are observed in this zone by the mineralogical composition, pore solution chemistry, and pore space geometry. A major part of the continental crust consists of relatively coarse-grained granite. Here, reactions at the mineral-water interface are lasting from the pedosphere to the lower base of groundwater.

In water-saturated pore systems under hydraulically stagnant conditions, the transport of elements is thought to be diffusion driven. Hence, studying diffusive transport is of fundamental importance in understanding the progress of weathering reactions, which are related with geochemical processes such as ion transport, mineral dissolution, and precipitation kinetics. Many studies on diffusive transport focus on clays, and the effective diffusion coefficient, D_{eff}, is used as a criterion to evaluate the design of barriers for waste disposals (Bourg et al. 2006). For granite, there are studies on diffusive transport from the viewpoint of geotechnique (Park and Baik 2009; Sato 1999; Xu et al. 2001), but also element turnover (Simonyan et al. 2009), whereas basalt is only rarely studied in this way (Navarre-Sitchler et al. 2009; Simonyan et al. 2012). The lowering of the effective diffusivity of solution components in porous rocks compared to the free liquid can be caused by morphology of the pore space, sorption processes of solution components on pore walls, and chemical reactions, e.g., dissolution of minerals and precipitation of secondary phases which consume or generate mobile species. Neglecting chemical rock/fluid interactions the most important parameters contributing to the diffusivity of solutions are the cross-sectional area of pores, tortuous diffusive pathway and the form of the pores.

Different methods for the determination of D_{eff} such as through-diffusion (Cormenzana et al. 2003) and in-diffusion techniques (Grathwohl 1998; Schampera and Dultz 2009) are used. In many studies on granitic rocks D_2O is used as a typical conservative, non-reactive tracer (Becker and Coplen 2001; Garcia-Gutierrez et al. 1997; Himmelsbacher et al. 1998). For basaltic samples, concentration profiles of the tracer Br^- were determined (Navarre-Sitchler et al. 2009). A prerequisite for the interpretation of such diffusion studies is the careful characterization of pore space in the rocks (Kaufmann 2009). Hg-porosimetry is a widely applied method to quantify pore size distributions from 1.7 to 100,000 nm. For characterization of pore space geometry different microscopic and tomographic techniques are used. Connective pores can be intruded with a low-viscous, fluorescence-doped resin (Schild et al. 2001) or a molten alloy (Dultz et al. 2006; Lloyd et al. 2009) and analyzed with different microscopic techniques. However, the intrusion of different pore sizes depends on the applied pressure and artefacts might appear, e.g., due to stress

release and when pore walls of unconnected pores break during intrusion. For the visualization of the 3-D pore space geometry, X-ray computed tomography as a non-destructive method was applied in studies on rocks (Navarre-Sitchler et al. 2009) and soil properties (Kaestner et al. 2006; Peth et al. 2008; Masaphy et al. 2009).

The scope of this work is to determine the role of pores for diffusive transport in two different magmatic rocks of widespread occurrence and high importance for element transfer, MOR basalts, and granites. Features for the formation of pores, pore volume, and the effect of pore filling with secondary minerals on diffusive transport are considered. In order to evaluate the role of porosity for the prediction of D_{eff} data on diffusive transport for the samples under investigation, porosity, and D_{eff} data for similar rocks reported in the literature are compared.

Study sites and sample selection

Mid-ocean ridge basalts (MORB), drilled samples from ODP leg 169 at Middle Valley, Juan de Fuca Ridge (leg 169, Hole 856H, 48°26′N, 128°40′W; PODP 1996), and dredged samples in the age from ca. 0 to 8.7 Ma from the East Pacific Rise at 14–16°S, 112°50′–106°30′W (Schramm et al. 2005) were investigated. The samples represent a sequence from fresh to completely altered basalts. Pillow basalts and basaltic flow from Juan de Fuca Ridge are moderately to highly altered aphyric to sparsely pyroxene- and/or plagioclase-phyric basalts. Hydrothermally alteration of primary minerals is generally extensive to complete. Rocks are altered to a cryptocrystalline intergrowth of quartz and chlorite with titanite. Water contents range from 4.5 to 7.6 wt% (Table 1), indicating, together with green tinting, significant chloritization.

Olivine and plagioclase-phyric and picritic basalts were recovered by dredging at East Pacific Rise. Alteration took place under seawater-dominated conditions at low temperature. The basalts show a general trend of increasing pervasive alteration with distance from the ridge axis. Rock interiors are generally characterized by low abundances of secondary minerals of <1 % (Schramm et al. 2005), whereas higher shares of secondary minerals are observed close to the surface, also indicated by higher water content (Table 1).

Rock fragments from granite and granite saprolites were sampled in the soil horizons of Podsols and podsolic Cambisols of two different sites in Germany: from the Harz Mountains (Oderteich (51°76′ N, 10°53′ O) and Drei Annen Hohne (51°77′ N, 10°71′ E) and the Black Forest (Höchenschwand, St. Blasien (47°74′ N, 8°17′ E) and Bärhalde (47°85′ N, 8°08′ E) at depth down to 2 m. The coherent partly weathered rock from Bärhalde was classified as weathered granite, whereas the disaggregated samples, where fabric and texture maintained, are classified as saprolites. In all samples orthoclase component (Or) and quartz have larger portions than plagioclase, which is always relatively rich in albite component (Ab). In the sample of Drei Annen Hohne vein perthite, probably formed during hydrothermal alteration, is present, where isotropy is given by an oriented texture of Or- and Ab-rich lamellae (Simonyan et al. 2009).

Methods

Pore volume, pore size distribution, and SSA

The selection of samples from the rock specimen was based on visual evaluation of the homogeneity and pore size distribution. Sections with large fractures were not included. The samples used for the experiments should represent typical specimen relevant for the weathering process. For basaltic samples sections from the surface and the core were sampled separately. With Hg-porosimetry, the percentage of open pores that are Hg-accessible was determined. Hg-porosimetry was carried out with a combined instrument (Pascal 140 + 440, POROTEC) for measuring macro- and mesopores in the range 58,000–1.8 nm radius. About 2 g of each sample were used. Longish sections oriented parallel to the surface were prepared from basalt samples and rock fragments mainly composed of feldspar with a diameter of 3-5 mm were segregated from granitic samples. First, the specimens were evacuated down to 200 Pa for 1 h to dry. Then the sample was immersed in the non-wetting mercury and pressure was incrementally increased up to 400 MPa while monitoring volume change. Hereby, the rate of pressure increase was automatically adjusted in an advanced procedure with lower rates at lower pressure levels and during measured intrusion processes. With increasing pressure, mercury intrudes into progressively smaller voids. A significant underestimation of pore size can arise if larger pores are accessibly through smaller pore entries only (so-called ink-bottle effect). In this case, the measured pore size represents rather the threshold size. The pore volume was derived from the quantity of intruded mercury. The pore size distribution was calculated using the Washburn equation, which gives a relationship between pressure and pore size (Washburn 1921).

$$r = -\frac{2\gamma\cos\Theta}{p} \qquad (1)$$

where r is the pore radius, p the pressure, γ the surface tension of mercury (0.48 N/m), and Θ the wetting angle of mercury (135°).

Table 1 Description of samples of mid-ocean ridge basalts and feldspar-rich samples from granite

Designation in text/ODP number, location	Rock type/soil horizon, depth (cm)	Porosity (%)[a]	Mean pore radius (nm)[a]	SSA (m²/g)[b]	Water content (wt%)[c]	Mineralogical composition[d]	Weathering degree	D_{eff} (m²/s)[e]
Mid-ocean ridge basalts								
Juan de Fuca ridge								
B1/0856 H-055R-1	Aphyric basalt, fine	8.3	13.8	3.4	7.1	Qz, Chl, Spn, Ilm	Complete	4.9×10^{-11}
B2/0856 H-057R 1	Phyric basalt, micro-crypto	18.1	40.1	3.0	7.6	Pl, Cpx, Qz, Chl, Spn, Ilm	Moderate to complete	n.d.
B3/0856 H-064R 2	Porphyritic basalt, crypto	13.3	240	1.0	4.5		High	n.d.
B4/0856 H-065R 1	Fine-grained basalt	8.3	29.3	2.4	4.9	Pl, Cpx, Qz, Chl, Spn, Ilm	Moderate-high	6.3×10^{-11}
East Pacific rise								
B5/20DS4 surface	Vesicular and plagioclase-phyric	4.8	54	0.4	0.61	Pl, Cpx, Ol, glass, Mag, Ti-Mag	Almost fresh	n.d.
B6/29DS2-surface		1.9	2	3.9	0.70	Secondary minerals (Schramm et al. 2005)	Almost fresh	n.d.
B7/36DS1-surface		7.5	4.5	2.2	0.44		Almost fresh	n.d.
B8/36DS1-core		4.0	2.3	3.1	0.47		Almost fresh	n.d.
B9/43DS9-surface		0.5	1.9	0.8	1.22		Almost fresh	n.d.
B10/43DS9-core		6.3	22.3	2.3	0.83		Almost fresh	7.1×10^{-11}
Granitic samples								
Harz mountains								
G1/Oderteich	Bv 30–60	19.3	172	0.78	0.83	Or, Qz, Pl	High	n.d.
G2/Oderteich	Cv 100–140	19.0	265	0.73	0.73	Ser, Kln, Gbs	High	2.8×10^{-10}
G3/Drei Annen Hohne	Cv 90–150	7.8	108	0.39	0.75	Or, Qz, Pl, Kln	High	5.8×10^{-11}
Black forest								
G4 Bärhalde	Aeh1 5–30	22.3	393	0.83	0.37	Qz, Pl, Or,	Moderate	n.d.
G5 Bärhalde	Cv 130–140	11.6	188	0.43	0.66	Ser, Kln	Moderate	7.7×10^{-11}
G6 Höchenschwand/St. Blasien	Cv > 200	12.3	225	0.41	0.26	Qz, Or, Pl	High	n.d.

[a] Porosity and mean pore radius (radius at 50 % of total pore volume) determined by Hg-porosimetry

[b] Specific surface area (SSA) measured by N_2-adsorption

[c] Water release >105 °C determined by Karl-Fischer-titration

[d] Abbreviations according to Whitney and Evans (2010)

[e] Data for D_{eff} are given for experiments carried out in the temperature range from 24 to 26 °C. Informations on total error and temperature dependency are given in Simonyan et al. (2009, 2012)

According to the shape of the intrusion curve with a quite flat slope, which indicates an increase of mercury penetration just according to the pressure and an extrusion curve, generally following the intrusion curve with a small hysteresis a conical pore geometry, which is common in rocks and soils was used to calculate the SSA of pores (Pascal, Thermo Finnigan 2002).

The SSA of the samples was determined by N_2-adsorption using the BET method (Brunauer et al. 1938). Each ∼1 g of a rock fragment was dried at 105 °C at a pressure $<10^{-3}$ mbar for a time period >24 h and was subsequently analyzed in the p/p_0 range from 0.05 to 0.3 (Quantasorb, Quantachrome). The validity of the measurements was checked in repetitions of selected samples.

Intrusion of a molten alloy

For the visualization of connected pore structures, a modified Hg-porosimetry technique was used utilizing instead of Hg a molten alloy called Wood's metal (50 % Bi, 25 % Pb, 12.5 % Zn, and 12.5 % Cd), which solidifies below 78 °C. Sections of rock samples with a length of ∼5 mm were transferred into cylindrical glass containers, located at the bottom of the tube with a stamp of steal to avoid floating, overlaid with molten Wood's metal and finally transferred in a temperature-controlled autoclave at 100 °C. The autoclave was evacuated <100 Pa. By applying an argon pressure of ∼55 MPa, the liquid metal was pressed into the accessible connective pores. According to the Washburn equation (1) using values of 400 mN m^{-1} for the surface tension σ of molten Wood's metal and 130° for the contact angle Θ between liquid and the pore walls (Darot and Reuschle 2003), pores with a diameter down to ∼20 nm are intruded, if connected to the surface. This pressure of 55 MPa was kept stable until solidification of the alloy, induced by cooling with liquid nitrogen. The high amount of Bi in the alloy counteracts the risk of shrinking during solidification (Hildenbrand and Urai 2003). Polished sections of intruded samples were examined with an environmental scanning electron microscope (ESEM; FEI, Quanta 200). Backscattered electron (BSE) images were recorded with an accelerating voltage of 15.0 kV, a spot size of 4.0 and a working distance of 10.0 mm. In the BSE images, pores intruded with Wood's metal appear typically bright.

Tomographic analysis of pore space

X-ray tomographic microscopy was performed at the TOMCAT beamline of the synchrotron light source of the Paul Scherrer Institute, Villigen, Switzerland. A series of projection images was recorded on cylindrical cores with a diameter of 2.1 and a height of ∼5 mm, which were drilled out of the rock samples with the longitudinal axis oriented parallel to the direction of drilling and for dredged samples perpendicular to the surface. The acquisition parameters for the projection images were an beam energy of 21.5 keV, an double-crystal multilayer (RuC on Si111 substrate) monochromator, an objective of 10×, an object to camera distance of 4 mm, an exposure time of 220 ms, an resolution of the charge-coupled device (CCD) of 14 bit/ pitch = 7.4 μm and an scintillating system with a LAG:CE 25 μm scintillator. Typically 1,200 images with a pixel size of 0.7 μm were recorded. The voxel resolution was $0.7 \times 0.7 \times 0.7$ μm and there was basically no distance between the layers. For tomographic reconstruction, a standard filtered back-projection routine with the Parzen filter was used (Huesman et al. 1977). Ring artifacts visible in the reconstructed slices have been mitigated by a two-step process in the sinogram domain, where these artifacts appear as straight lines, parallel to the theta axis. After a low-pass filtering approach, anomalous lines have been detected thanks to their low variance and smoothed through linear interpolation.

The images were digitized in 256 gray levels in arrays of 1,024 pixels edge length. Gaussian filters of different sizes were used for preprocessing and smoothing of the images. To image and quantify pores, the grayscale histogram was segmented. The software used in the segmentation process was the OpenCV library. Basically, the segmentation step starts by smoothing the images using a Gaussian filter. Afterwards color threshold takes place. Finally, the outputted information is binarized.

Images of the pores were created by displaying the border pixels of the separated pores. Pore volume and pore size distributions were calculated. Main directions of pores in the cylindrical samples were calculated in the 3-D orthogonal system by a principal component analysis (PCA). Using the covariance matrix (A) of the whole set of x-, y-, z-coordinates of all binarized voxels of the probe, it is possible to calculate eigenvectors (v) and eigenvalues of A by using the singular value decomposition SVD method (Kalman 1996). The eigenvectors $v1$, $v2$, $v3$ present the directions of the three principal axes of all points, where the vector with the highest eigenvalue gives the main direction of the voxel-set, meaning that it explains most of the variance in the dataset. Low eigenvalues show small variances in the datasets in the corresponding direction. Strong differences in eigenvalues within the 3-D orthogonal system would indicate a marked anisotropy of main direction of pores, which most probably induce spatial variability in transport.

Weathering degree

Samples were separated with respect to the weathering degree in four different grades (fresh, moderate, high, and complete) based on porosity, water released above 105 °C

and portions of secondary minerals. Assuming that the alteration produces secondary porosity due to decomposition of primary minerals, porosity is a parameter for the weathering degree in rocks, which have initially the same pore volume.

For determination of the water content as a relative measure of the abundance of secondary formed layer silicates, samples were transferred into a Karl-Fischer-titration (KFT) apparatus and slowly heated to 105 °C and then faster (100 °C/min) to 1,300 °C and the titration rate was continuously measured as a function of temperature. The titration was terminated by the dead stop method (Behrens 1995). Portions of secondary minerals in polished sections

were estimated on the basis of their relative abundance using electron microscopy.

Results and discussion

Structure of connective pores

In the overview BSE images of the fresh basalt B10 and moderately altered basalt B4 relatively homogeneously distributed porosity in sections embedded in the solidified alloy can be seen (Fig. 1a, d). Pores in the rocks appear well connected and high shares of the SSA are located
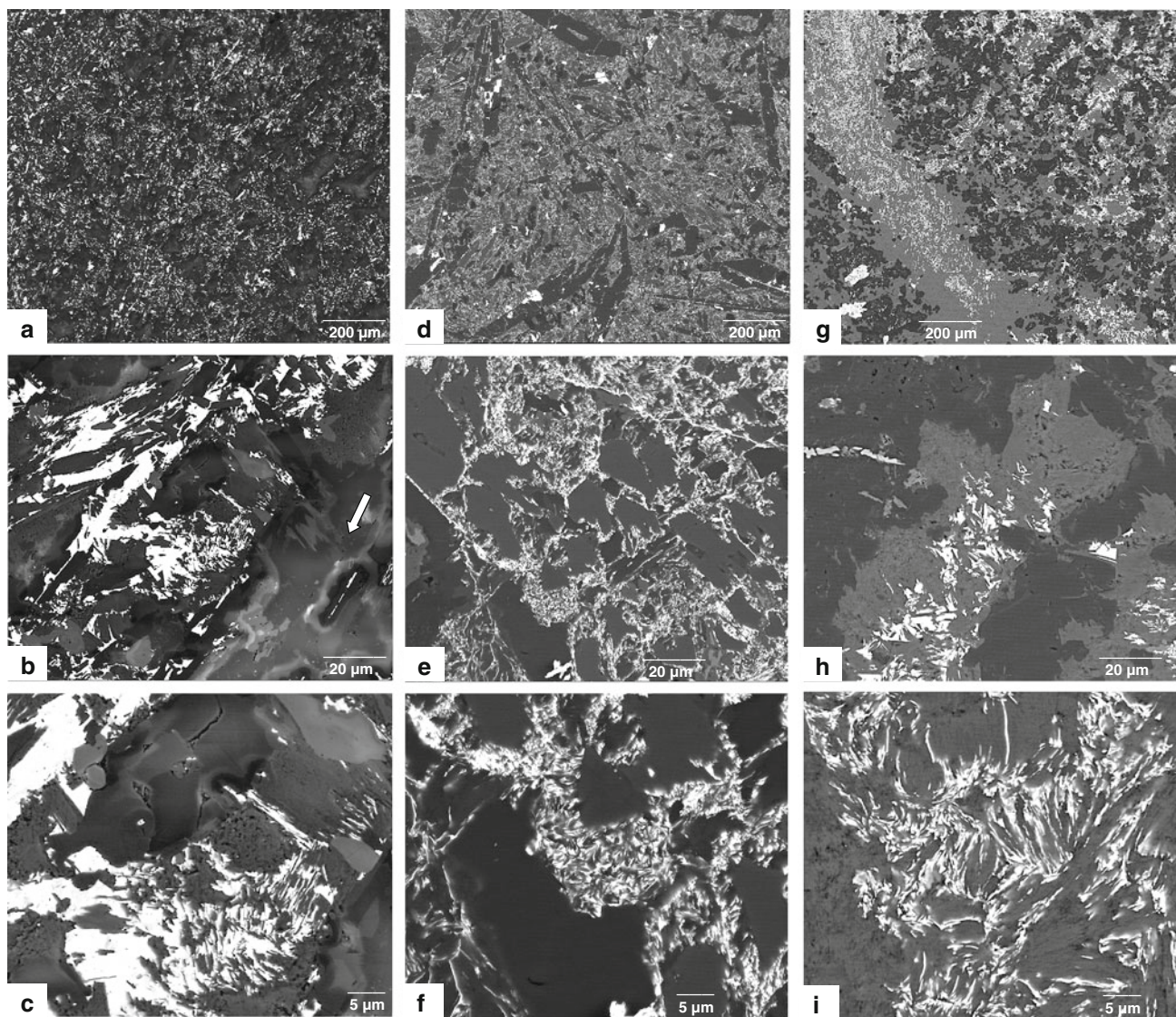

Fig. 1 Backscattered electron images showing the pore network in polished sections of differently altered mid-ocean ridge basalt samples. The connective pore system, intruded by a molten alloy is appearing *white*. **a–c** Fresh sample B10 containing glass (*white arrow* in **b**), **d–f** moderately altered sample B4 with chlorite and mica in the pores (**e, f**), **g–i** completely altered sample B1 with cryptocrystalline intergrowth of quartz (*dark-gray*) and chlorite (*gray*)

inside rock fragments emphasizing that transport from solution constituents for mineral weathering might be a rate-limiting step. At higher magnification of the fresh basalt, glass is also visible in the groundmass (Fig. 1b, c). No secondary minerals can be observed in the pores visualized in BSE images, indicating that alteration under seawater-dominated conditions at low temperature was relatively weak, despite of the age of 8.5 Ma of this rock. This finding is supported by the fact that the water content of this sample is relatively low (Table 1). A strong tortuosity of the pore system can be assumed from the orientation of the bright appearing connected pores in Fig. 1b, c. Some black appearing pores visible at high magnification represent voids in the sample not intruded by the molten alloy. On the one hand, these pores can represent non-connective (closed) pores, on the other hand not all connected pores may be intruded. According to the Washburn equation (Eq. 1) all the pores with a diameter larger than 20 nm should be accessible by the applied 55 MPa pressure. However, the calculation has uncertainties because the Washburn equation is only valid for cylindrical pores and also surface roughness and the presence of bottle neck pores hinder accurate intrusion. Filling of large volumes in the interior of rock samples may be not possible/incomplete if transport through narrow pore systems is required, i.e., the flux may be hindered somewhere on the patchy narrow pore transitions.

A well-connected pore system can also be observed in the overview BSE image of the moderately altered basalt, where phenocrysts of plagioclase are clearly visible by their relatively low porosity in comparison to the groundmass (Fig. 1d). At higher magnification layer silicates, consisting mainly of chlorite and mica are clearly visible in the pores (Fig. 1e, f). The presence of layer silicates is probable of high importance for transport, as pathways for diffusion are narrowed not only by the platelets itself but also by a bound water layer on the external surface, where diffusive transport is slowed down and which effectively decrease pore space (Kozaki et al. 2001).

The transformation of primary minerals is almost complete in basalt B1. Quartz and chlorite together with some titanite were observed. High shares of chlorite are also indicated by the relatively high water content of the sample (7.1 %, Table 1). Quartz and chlorite have a patchy distribution in the sample. Obviously the intrusion of the molten alloy is incomplete, which is due to high shares of layer silicates, increasing the number of small pores which are not intruded. In the BSE image with a magnification of 5,000× (Fig. 1i) it can be seen that the orientation of pores is clearly related to foliation due to crystallization of chlorite.

Extended connective pore systems are also observed in the samples from granite (Fig. 2a–h). In the BSE image of samples G1 and G2, porosity developed preferentially in the albite (Ab)-rich feldspars forming a patchy distribution. Encapsulated quartz did not hinder the intrusion of the molten alloy. At higher magnification, secondary minerals, mostly kaolinite and gibbsite can be observed by SEM in pores of samples G1 and G2 (Fig. 2b, c), but not in the other samples from granite (Fig. 2f, h). Whereas in the completely altered basalt sample B1 (Fig. 1i), secondary minerals strongly hinder the intrusion of the molten alloy, this is not observed for sample G1 and G2, where big connective pores are observed in the whole matrix and intrusion is only limited at few sites, where dense packing of secondary minerals are present (Fig. 2c). Relatively large black appearing voids visible in Fig. 2a are attributed to preparation due to fragility of these highly porous samples.

In the BSE images of a vein perthite of sample G3, a streaky almost regular pattern of pores intruded with bright shining alloy is observed (Fig. 2d–f). At higher magnification, the orthoclase (Or)- (light-gray) and Ab-rich phase (dark-gray) can be distinguished by their gray shade (Fig. 2e, f), whereby porosity formed preferentially in the Ab-rich phase. At larger magnification (Fig. 2f), some black appearing voids in the section can be also observed representing closed pores or pores, which were not intruded. It cannot be excluded that some of these pores are connective pores because the accessibility of pores for Wood's metal is limited to radii larger than 10 nm.

In BSE images of rock fragments from Bärhalde granite (G5), the larger porosity of Na-rich plagioclase compared to alkali-feldspar is clearly visible, illustrating the higher susceptibility of this feldspar to weathering (Fig. 2g, h). Porosity is also due to cracks and observed along grain boundaries, whereby some of the pores propagated from cracks into the feldspar.

Porosity and pore size distribution

Pore volumes of MORB samples determined by Hg-porosimetry vary between 0.5 vol.% for the dredged basalt B9 and 18.1 vol.% for the drilled basalt B2 (Table 1). The high variability is due to different extents of degassing reactions during discharge of the magma but depends also on the weathering degree. Samples of the East Pacific Rise have lower porosity than those from Juan de Fuca Ridge, indicating that the formation of secondary porosity under seawater-dominated conditions is limited. The low porosity of sample B9 stemming from the core of a basalt fragment can arise from the fact that pores are filled with Fe-oxides and different layer silicates (Schramm et al. 2005), also indicated by the highest water content of all dredged samples (1.22 wt%). Strongly weathered MORB samples do not have porosities below 8.3 vol.%.
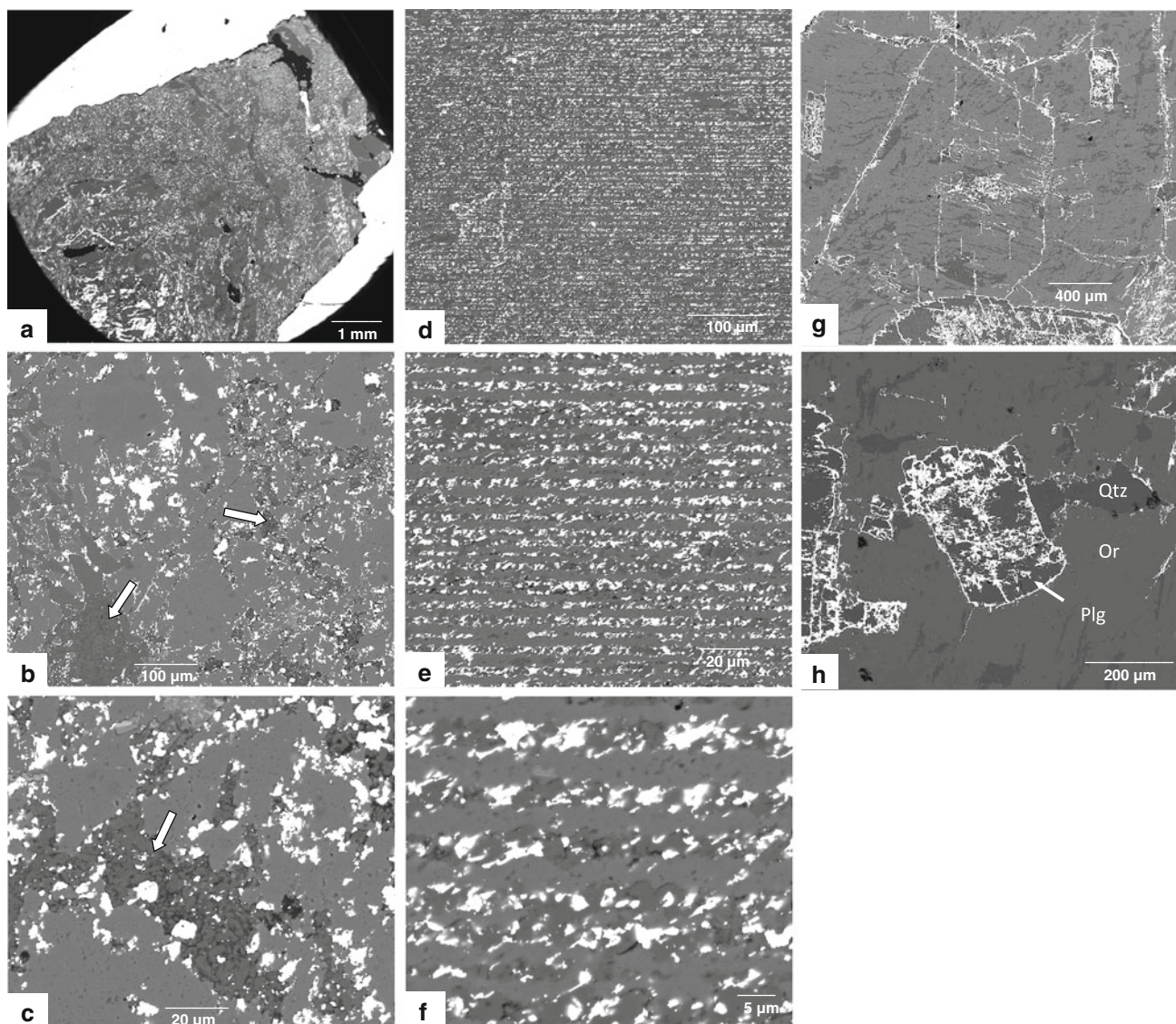
Fig. 2 Backscattered electron images of pore networks in polished sections of different granitic samples. The alloy "Wood's metal" appears white marking the connective pore system. **a–c** Granite saprolite G2 with kaolinite in pores (*white arrows* in **b**, **c**), *black* appearing sections in **a** arise from voids due to preparation, **d–f** perthitic feldspar from G3 with the bright shining alloy in pores within the *dark-gray* albitic lamellae. The Or-rich phase appears *gray* and voids *black* (**f**), **g**, **h** Granite G5

For the granitic samples, relatively high porosities varying from 7.8 vol.% for a perthitic feldspar grain from Drei Annen Hohne (G3) to 23.7 vol.% for a feldspar-rich rock fragment from Bärhalde (G4) were observed. The highest value in the latter sample G4 is attributed not only to mineral dissolution but also to the presence of cracks (Fig. 2g). The fact that in feldspars from plutonic rocks, a porosity of ~1 vol.% is typical (Brantley and Mellott 2000) indicate that the feldspar-rich samples under investigation are strongly affected by weathering and/or stress relaxation (Schild et al. 2001).

In general, feldspar-rich granitic samples have a higher share of coarse pores than MORB samples (Fig. 3a, b).

High shares of pores are between pore radii in the range from 100 to 1,000 nm, also indicated by the position of the inflection point of the curves marking the maximum in pore size distribution. With exception of the highly weathered sample B3, maxima in pore size distribution for MORB samples are below a pore radius of 100 nm. MORB samples show a tendency to bimodal distribution with a second maximum in pore size in the range of some nm. This is assigned to the widespread occurrence of layer silicates in the samples, which causes the formation of fine pores. In opposite, pore size distribution in granite samples is more homogeneous. Five of six granite samples show one broad maximum of pore radii between 80 and 390 nm (Fig. 3b).
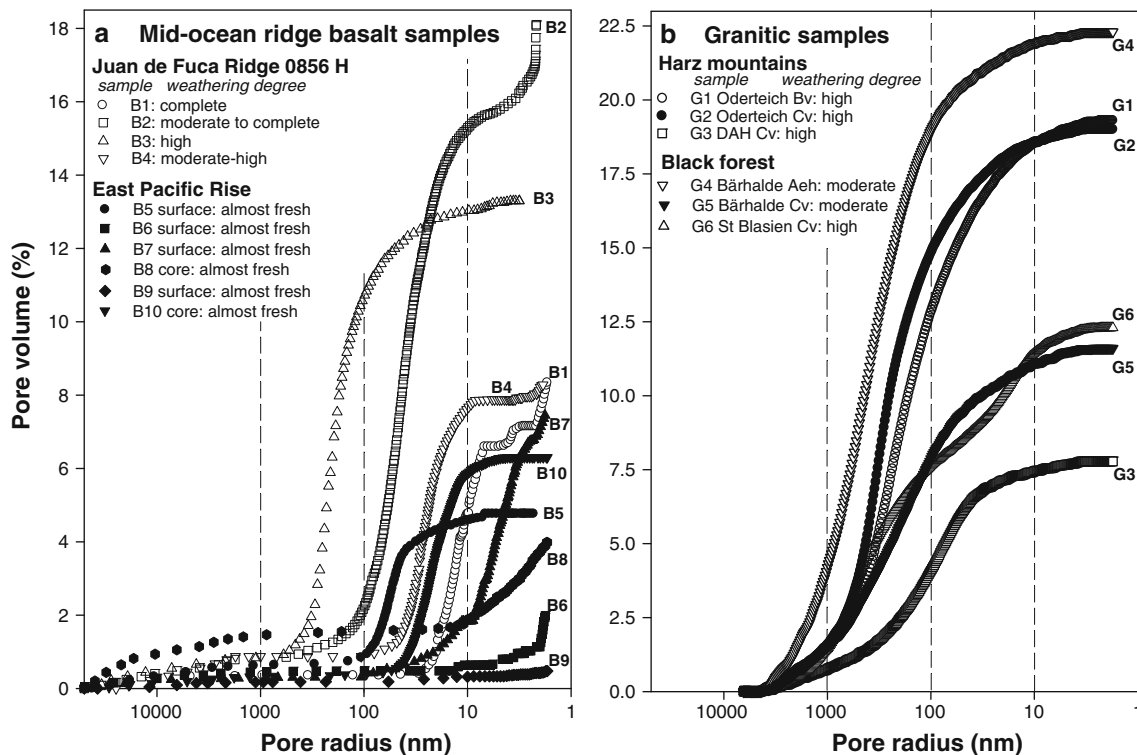
Fig. 3 Cumulative curves of pore size distribution of differently altered mid-ocean ridge basalts (**a**) and granite samples (**b**) determined by mercury intrusion porosimetry

For G6, two wide maxima at 20 and 540 nm are found. Only a few pore radii are larger than 1 μm. Indication that secondary minerals are present in granite samples in minor amounts only is also obtained from the SSA analysis, where granitic samples have SSA values less than 0.8 m^2/g but MORB samples up to 3.9 m^2/g. SSA values from Hg-porosimetry are typically much higher than values from N$_2$-adsorption, which is assigned to an overestimation of small pores by Hg-porosimetry.

Pore structure by X-ray tomographic microscopy

For tomographic analysis, almost fresh, moderate, and completely weathered basalt samples (B1, B4, and B10) having a similar pore volume (6.3–8.3 vol.%), and for comparison a perthitic feldspar separated from a granitic rock fragment (G3) with a streaky almost regular pattern of pores and a pore volume of 7.8 vol.% were chosen.

The images digitized in 256 gray levels (Fig. 4b) in arrays of 1,024 pixels edge length were interspersed with noise caused by the physical property of the X-ray tomography apparatus (Fig. 5a). No separate gray values for the pores and different minerals in the sample can be observed in the original grayscale histogram (Fig. 4b). Therefore, 2-D Gaussian filters of size 11 × 11 (B10), 15 × 15 (B4, B1), and 23 × 23 (G3) pixels were used for

preprocessing and smoothing of the images (Fig. 4c, d). Different filter sizes were used to avoid irrational high numbers of separate pore systems. The bigger the size of the kernel (filter), the smoother the image will be, meaning that smaller pores will disappear.

The effect of smoothing of images is shown in Fig. 5 for an array of 50 × 50 voxels. The original image is strongly infiltrated with noise and apparently unsystematically voxels of different gray tones appear in direct vicinity (Fig. 5a). As crystals of feldspar and pyroxene in the sample are much bigger than the dimensions of a voxel, regions with similar gray tones should be expected.

Using the Gauss filter, a smoothing was obtained and regions of voxels with coherent gray tones representing different minerals and pores could be separated (Fig. 4b). Pores have the lowest gray tones and appear dark-gray (exemplified by white arrows in Fig. 5b), whereas feldspars appear gray and pyroxenes bright gray. The voxels assigned to pores can be derived from the final image after application of a threshold (Fig. 5c).

In all samples under investigation, no separate maxima of gray values for pores and different minerals can be observed in the original grayscale histogram (Fig. 6a–d). After application of the Gauss filter, different mineral phases could be separated in all basaltic samples of different weathering degree (Fig. 6a–c) in the grayscale histogram.
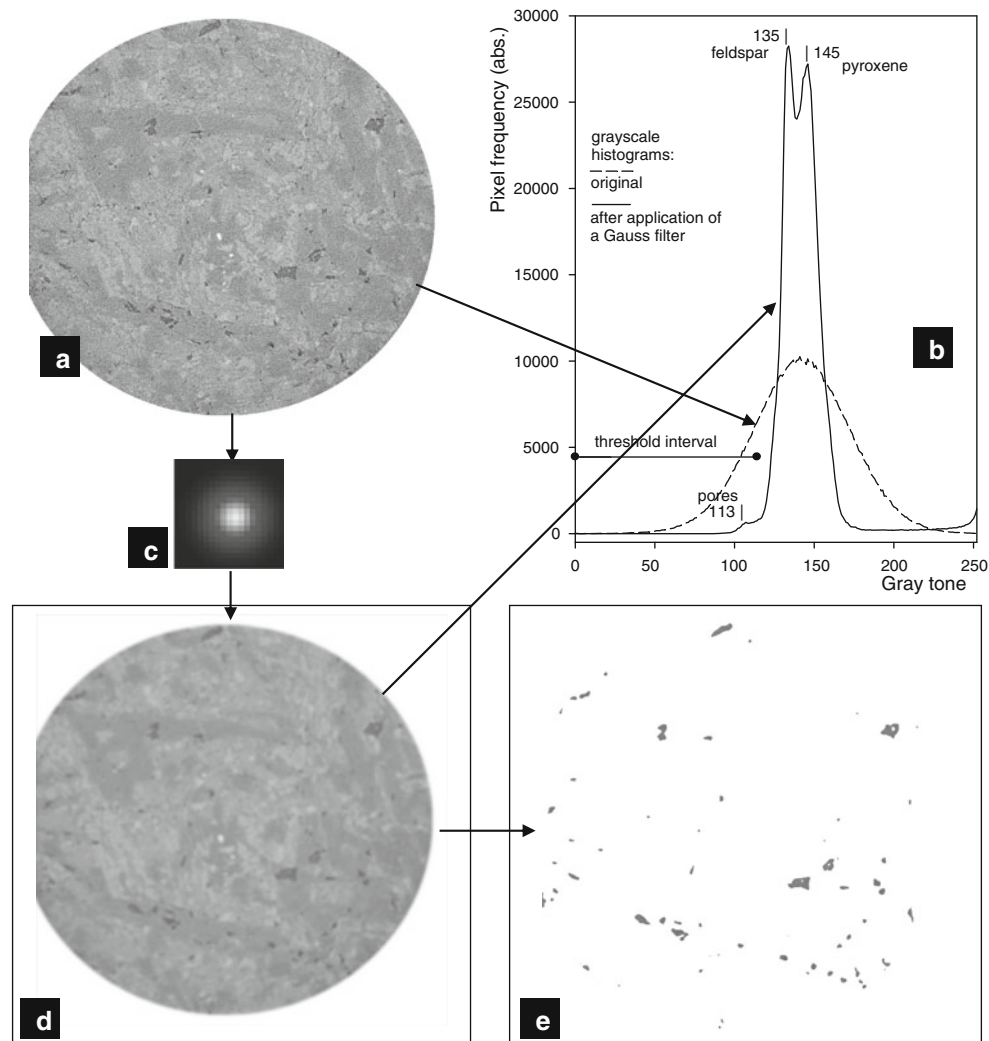
Fig. 4 Image analysis of a layer obtained by X-ray tomography, demonstrated for the moderately altered basalt sample B4: Image of a layer obtained by X-ray tomography (**a**) and corresponding grayscale histogram (**b**, *dashed line*). Gauss filter mask 21 × 21 pixel (**c**) and the resulting image (**d**) with the corresponding grayscale histogram (**b**, *solid line*). By application of a threshold from gray tone 0-117 the pores in the layer are separated (**e**)

To image and quantify pores, the grayscale histogram was analyzed in the following way: the pores were given by gray tone values left of the first clear peak, which can be assigned to a mineral. If another local maximum was found on the left side, then the local minimum in between the two peaks was established as the threshold (Fig. 6b). If there is no visible local maximum within the pore range, then the threshold was calculated by adding the highest gray value (coming from 0), which surely characterizes pore structures in different image layers of the probe, and the gray value of the first clear peak in the histogram. This sum is then divided by two to get the threshold for the pores (Fig. 6d). Higher gray tones were assigned to minerals. The number and size of identified pore structures is clearly affected by the position of the upper threshold. For sample B10, the reduction of the upper threshold by two gray tones from

120 to 118 resulted in a decrease of calculated pore volume by 10 %, whereas it increased by 12 % if the threshold was shifted to a gray tone of 122.

Calculation of 3-D images in circular arrays with a diameter of 1,024 pixels resulted in a relatively high number of separate pore systems which is in opposite to the findings by Wood's metal intrusion, where pores were observed to be well connected. 89 separate pore structures/million voxels were obtained for completely altered MORB sample B1 and 219 for the almost fresh MORB sample B10 (Table 2). Obviously the X-ray tomographic microscopy approach, even performed with a relatively high spatial resolution of 0.7 μm pixel width, is not sufficient to resolve all parts of the pore space. The pixel width appears to be a key point in the tomographic approach and it can be assumed that pores with a pore diameter quite
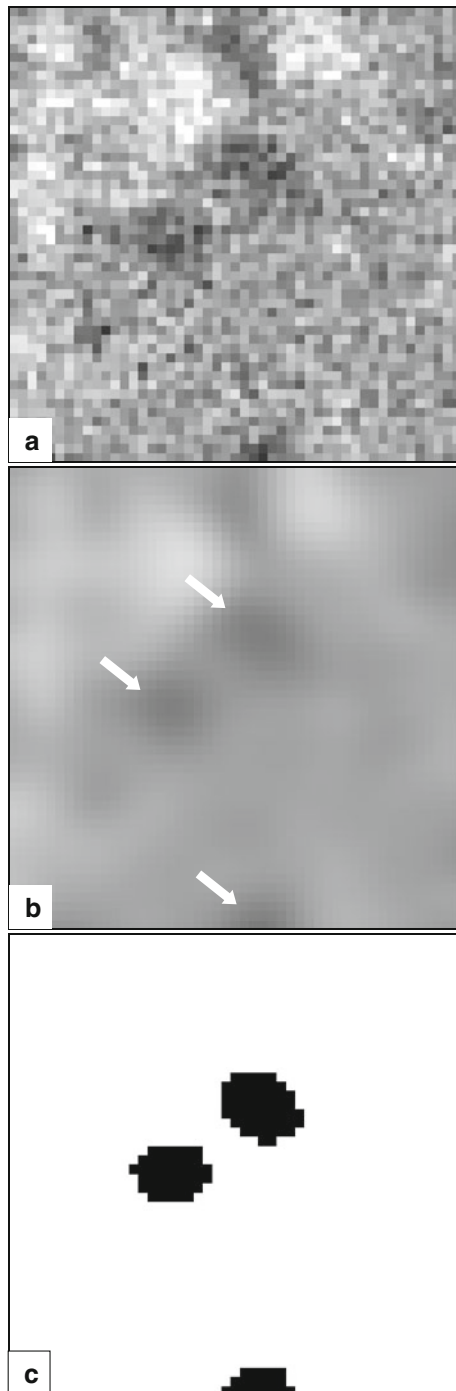
Fig. 5 Distribution of gray tones for an array of 50 × 50 voxels in the original tomographic image of a layer of almost fresh basaltic sample B10 (**a**) and the same array after smoothing with a Gauss filter (**b**) and the final image showing the voxel assigned to pores after application of a threshold (**c**)

smaller than the pixel size will not have a significant effect on the gray value of the pixel and hence cannot be visualized with this method. However, this is a general problem of all image based approaches, which focus their analyses on specific areas and spaces.

According to mercury porosimetry especially MORB samples have high shares of pores below a pore radius of 0.1 μm (Fig. 3a), suggesting that only the coarser fraction of pores is imaged by tomography. Out of this reason, relatively high numbers of separate pores were observed and porosity, quantified by tomography tends to be underestimated, most pronounced for the completely altered MORB sample B1 with a high share of fine pores and the highly weathered perthitic feldspar sample from granitic rock G3. Here more sophisticated methods such as focused ion beam nanotomography (Keller et al. 2011) may help to improve visualization of fine pore structures.

The largest pore structure is observed in the fresh basalt sample B10, which has almost 0.71 million voxels within the 636 million voxels imaged. Here, it has to be considered that pore systems are cut at the edges of the cylindrical array determined and might have a much larger extension. The size of a pore structure at a pore volume of 50 % is from 699 voxels (240 μm^3) for sample G3 to 12,595 voxels (4,320 μm^3) for sample B10 (Table 2). The finding of the largest pore structure in fresh basalt B10 together with the highest porosity determined by tomography in basalt samples is most probably due to the fact that the absence of layer silicates in the pores eases their identification (see paragraph above).

Images of the separated pores were created by displaying the border voxels, showing the maximum extension of the identified pores in the cylindrical array (Fig. 7a–d). This kind of presentation allows the best view on pore systems detected. 3-D pore distributions imaged in Fig. 7 are quite different within the four samples. The most homogeneous distribution is observed for the almost fresh MORB sample B10 (Fig. 7a). With increasing weathering degree from sample B4 (moderate-high altered MORB, Fig. 7b) to complete altered MORB (sample B1, Fig. 7c) pore distribution appears increasingly heterogeneous, indicated by stronger differences in the density of imaged border voxels. The heterogeneous distribution of pores might be assigned to dissolution and reprecipitation processes, which concentrate pores in certain areas. This might be driven by the fact that secondary minerals can form not only in direct vicinity to the weathering mineral but also in any distance.

The habitus of the pores in a perthitic feldspar from granitic sample G3 appears in the 3-D image streaky with a regular pattern of pores which remind to the BSE images (Fig. 2d–f). Porosity along the albitic lamellae can be clearly traced in the 3-D image. Despite this observation, main direction of pores calculated by PCA do not have the same orientation as suggested from BSE images of perthitic feldspar sample from G3. Also second and third linear combinations which explain the maximum proportions of the remaining variance acted from the pores, are not
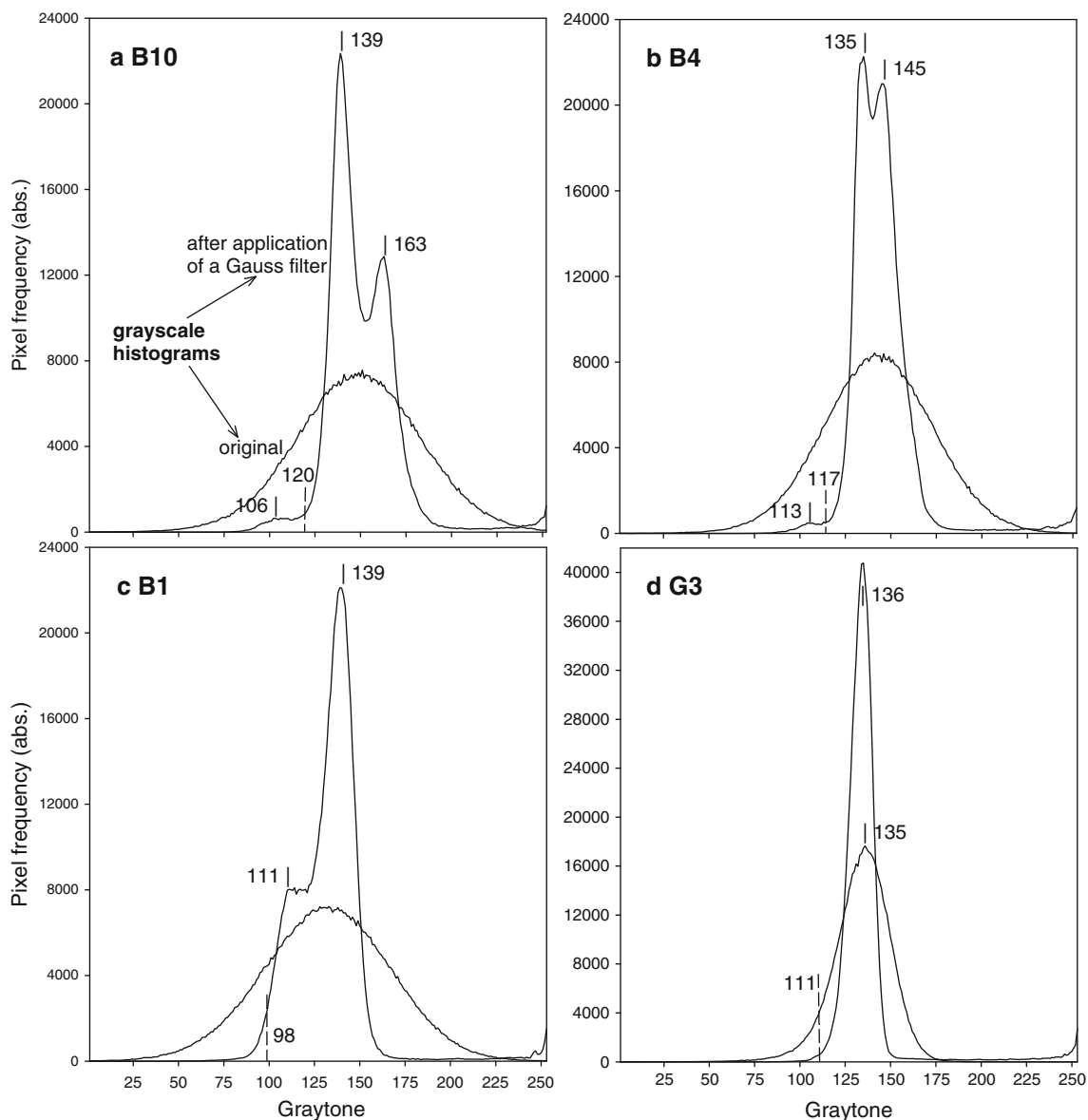
Fig. 6 Grayscale histograms of tomographic images of layers of almost fresh (**a**), moderate-high (**b**) and completely (**c**) weathered basaltic samples and a perthitic feldspar sample (**d**) before and after application of a Gauss filter. The *dashed line* marks the upper value of gray tone in the threshold interval starting with zero

Table 2 Pore space characteristics derived from data of tomographic analysis

	B10	B4	B1	G3
Porosity by tomography (%); in brackets: porosity by MIP (%)	3.54 (6.3)	1.89 (8.3)	0.99 (8.3)	0.67 (7.8)
Number of pore structures (pore structures/million voxels)	219	53	89	57
Number of voxels in a separate pore structure at a pore volume of 50 %	12,595	8,369	10,065	699
Biggest connective pore structure (number of voxels)	712,354	500,880	379,621	310,355
Eigenvalue of vector $v1$	88,440	84,626	89,988	94,175
Eigenvalue of vector $v2$	59,459	52,613	74,773	59,459
Eigenvalue of vector $v3$	48,147	44,525	42,924	48,147

Fig. 7 Perspective view from the side on 3-D microstructure of pores in cylindrical arrays with a diameter of 700 μm visualized by X-ray tomographic microscopy of fresh basalt B10 (**a**), moderately altered basalt B4 (**b**), completely altered basalt B1 (**c**) and perthitic feldspar from granite G3 (**d**). Exclusively the pores are imaged in the cylindrical array whereas the minerals appear transparent. The scale is one pixel with a size of 0.7 μm. The height of the cylindrical array is 840 μm and the diameter 700 μm. For better visualization of the separated pores, the border pixels are displayed only and the image was stretched in z-direction. The three axes represent the main direction of pores in the 3-D orthogonal system with eigenvalues decreasing in the order *black* (axis 1) > *green* (axis 2) > *blue* (axis 3)
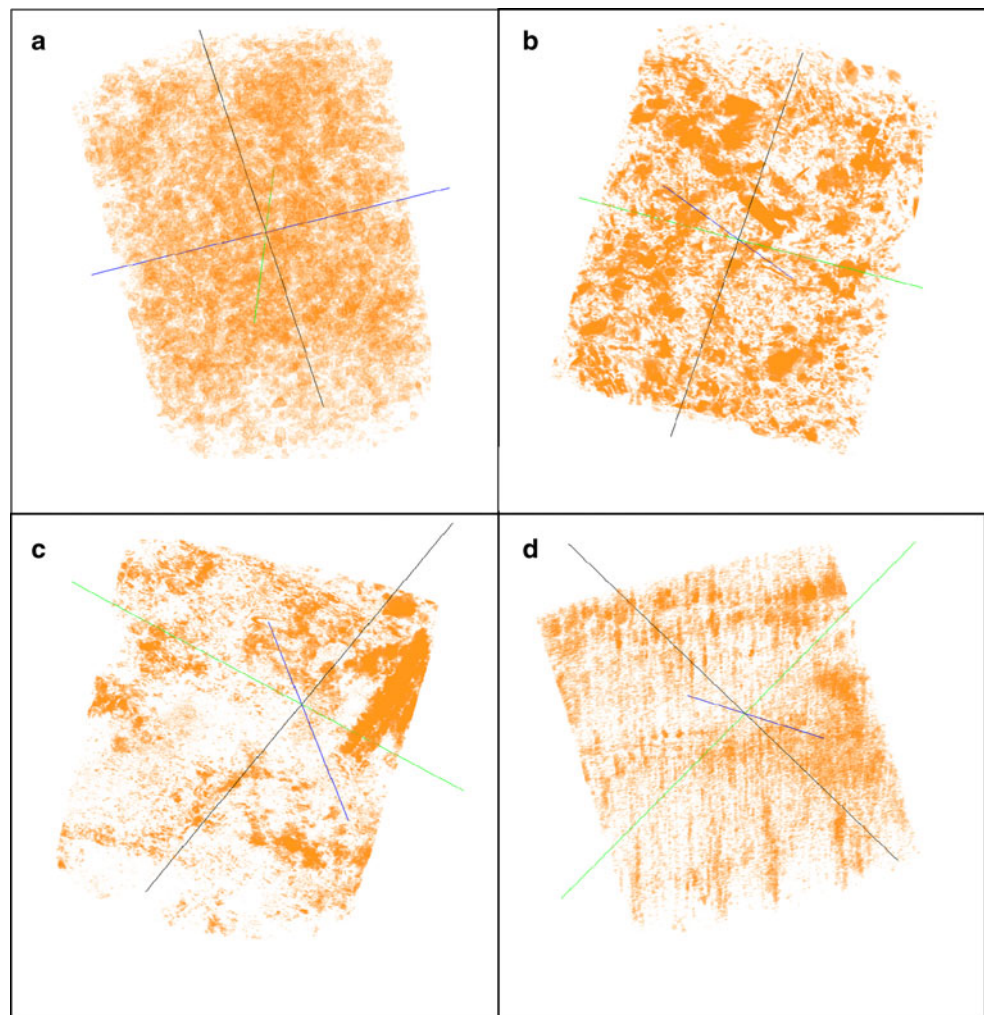
oriented along the main direction of pores derived from electron microscopy. The variance in the pore distribution for the given factor (main direction of pores), accounted by the eigenvalue, is clearly ordered in the 3-D orthogonal system, ranging from 94,175 for V1 to 59,459 for V2 to 48,147 for V3 (Table 2). The weakest ordering between V1 and V2 is observed for completely weathered sample B1. The determined differences in eigenvalues within the 3-D orthogonal system of the samples indicate a slightly anisotropy of pores. For porous perthitic feldspar spatial variability in transport was obtained. Diffusion parallel to the lamellae was about 0.4 log units slower than perpendicular to the lamellae (Simonyan et al. 2009). Spatial variability in transport in clays can be much stronger because of the strong preferred orientation of pore paths within the bedding plane (Keller et al. 2011).

Relation between porosity and diffusive transport

Determination of the effective diffusivity of water of the samples from this study reveal, that D_{eff} is controlled by physical factors of the rocks like porosity, pore connectivity, pore geometry, and distribution (Simonyan et al. 2009, 2012). For basaltic samples, at almost the same porosity diffusion in completely altered basalt with a high content of layer silicates is 0.4 log units slower than in almost fresh and partly altered basalts. Despite this visible effect of pore size on D_{eff}, porosity appears to be the most decisive factor for diffusive transport in these two rocks. As this parameter is considered in most studies in literature, here effects of pore space characteristics on diffusive transport were analyzed via comparison of porosity and D_{eff} for H_2O and compounds with comparable diffusivities. The data set includes samples from basalts and granites of this study, investigated by $H_2O \rightarrow D_2O$ exchange experiments, and studies on similar rocks reported in literature. Considering the temperature dependence of diffusion, only data from experiments carried out in the temperature range from 18 to 26 °C were taken into account. Pore volumes ranging from 0.6 to 30 vol.% for basaltic and 0.04 to 14 vol.% for granitic rocks were considered. As the diffusivities of H_2O and D_2O are comparable to those of

monovalent cations and anions (Li and Gregory 1974), D_{eff} obtained with non-sorbing tracers such as Br^- (Navarre-Sitchler et al. 2009), I^- (Benning and Barnes 2009), and HTO (Sato et al. 1997) were included.

The diffusion within the porous media is mainly controlled by the increase of the path length of diffusive species due to tortuosity and the obstruction of diffusion due to the pore constriction. These effects can be described in terms of the diffusional tortuosity factor X. The mass transfer through a porous membrane is additionally affected by the change of the effective diffusive cross-section, i.e., the ratio of the cross-section available for diffusive permeation to the bulk cross-section. This ratio corresponds to the bulk porosity Φ (Dullien 1992).

Data of D_{eff} considered in this study were obtained on the one hand in the laboratory applying in- or through-diffusion techniques with non-sorbing tracers (Navarre-Sitchler et al. 2009; Simonyan et al. 2009; Widestrand et al. 2007) and on the other hand on a theoretical basis using analytical and semianalytical solutions to Fick's law for the typical through-diffusion experiment, applied for determining effective porosities and D_{eff} from through-diffusion experiments (Benning and Barnes 2009). D_{eff} obtained on a laboratory and theoretical basis are shown separately in Fig. 8. The rock capacity factor, reported in studies where D_{eff} is determined on a theoretical basis for non-sorbing diffusing species is equivalent to the interconnected porosity.

D_{eff} determined on different granitic materials including fine and coarse-grained granites as well as porphyritic granites to granodiorites were considered (see references in Fig. 8a). The availability of data for D_{eff} on basaltic samples is more limited and no data at bulk porosity $\phi < 0.006$ are available. Out of this reason in addition to the differently altered MORB samples, results from a weathered basalt clast, an altered breccia of aphanitic basalt fragments with zeolites and chalcedony distributed throughout, and breccias with lithic basalt fragments ranging in size from 1 mm to 3 cm in a clayey matrix (Benning and Barnes 2009) were included (see also references in Fig. 8b).

The relationship between D_{eff} and ϕ, the rock capacity factor determined on a theoretical basis (Lever and Bradbury 1985) and experimentally measured porosity is shown simultaneously for samples from granitic and basaltic rocks in Fig. 8. The parameter ϕ in Fig. 8 represents both, the rock capacity factor and the porosity. D_{eff} increases more steep with increasing ϕ for basaltic than for granitic samples. At the same ϕ diffusive transport in basalt appears to be much slower than in granite. The linear regression correlation obtained in the log–log space was found to be with $R^2 = 0.58$ for granitic and $R^2 = 0.61$ for basaltic samples of almost the same value. Despite the fact that only data determined on an experimental basis were considered for the linear regression, the coefficient of
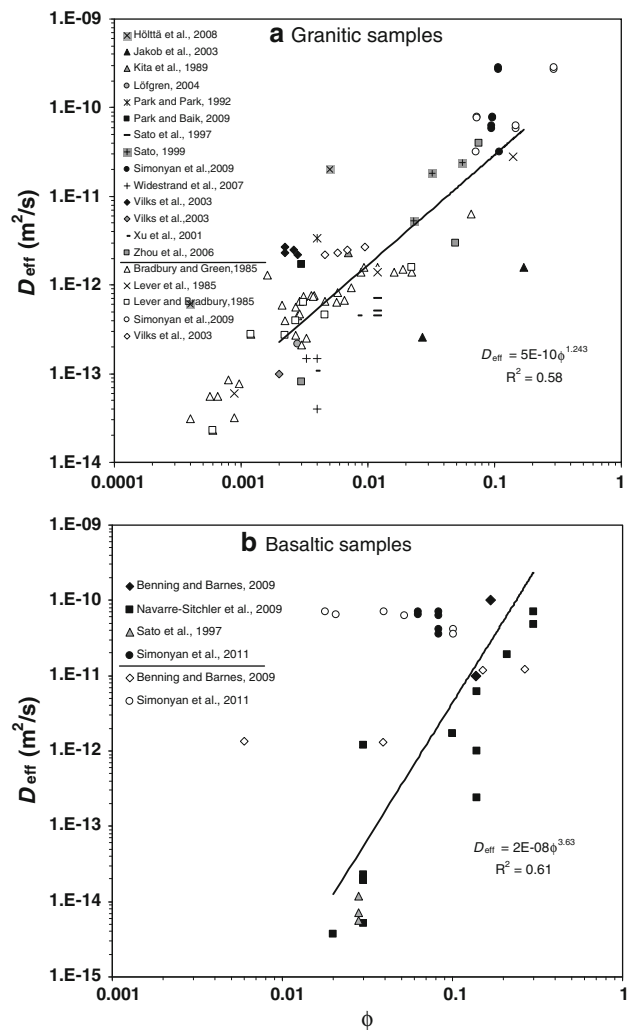

Fig. 8 Determination of the validity of the parameter ϕ (rock capacity factor determined on theoretical basis and measured porosity) for the prediction of D_{eff} in granitic samples (**a**) and basaltic samples (**b**) in linear regressions. Note that *open symbols* below the line in the list of literature indicate D_{eff} which were determined on a theoretical basis, whereas the other data are D_{eff} determined on an experimental basis. Data determined on theoretical basis were not considered for the linear regression. Included were data from samples under investigation and literature. Only data from experiments carried out in the temperature range from 18 to 26 °C were included. In most studies I^- is used as a tracer, also Br^- (Navarre-Sitchler et al. 2009), Cl^- (Kita et al. 1989; Sato, 1999), H_2O/D_2O (Simonyan et al. 2009, 2012), HTO (Jakob et al. 2003; Sato 1999; Widestrand et al. 2007), Na^+ (Jakob et al. 2003; Kita et al. 1989; Sato 1999), and Cs^+ (Park and Baik 2009; Park and Park 1992; Sato 1999; Sato et al. 1997; Widestrand et al. 2007; Xu et al. 2001)

determination indicates that the prerequisites for the prediction of D_{eff} from porosity are relatively poor for both rocks, limited to a precision with an average error ± 0.38 log units for granitic and ± 0.74 log units for basaltic samples.

For the observed variability it has to be considered, that the data included stem from rock species from granite and

basalt with different properties decisive for the value of D_{eff} such as pore size distribution, tortuosity of diffusive pathways, and kind of minerals formed. In addition, there is a small-scale variability of parameters significant for diffusion in rocks which also affects transport (Huysmans and Dassargues 2012). Data points shown do not necessarily imply representativity for granites and basalts in general and most probably the relation between porosity and D_{eff} would be much stronger, if samples with similar properties are considered only. This can be seen from diffusion experiments carried out on samples from one source rock using the same method (Navarre-Sitchler et al. 2009).

The observed variability may also have methodical reasons as different techniques for diffusion experiments, through- and in-diffusion methods with different distances, ranging from 1.2 mm to 30 m were applied. In order to get representative diffusion data for the rocks, the distance for diffusion should be large. Some uncertainties can arise also from different methods for determination of porosity, e.g., Hg-porosimetry is based on a model assuming cylindrical pores, which is not correct in presence of layer silicates in the sample. Here, it has to be considered to include only data in such a regression analysis stemming from the same methodological approach.

From the comparison of diffusion data determined on an experimental and theoretical basis, respectively (Fig. 8), no systematic differences between the two methods can be deduced as the variability is relatively high. At lower ϕ, the difference of D_{eff} between basaltic and granitic samples is strongly increased. Whereas at a ϕ of 0.1, D_{eff} is 1.8×10^{-11} m^2/s for granitic and lower with 3.8×10^{-12} m^2/s for basaltic samples, differing by a factor of ~ 5, at $\phi = 0.01$ D_{eff} is for granitic samples 1.0×10^{-12} m^2/s and almost two orders of magnitude lower (2.8×10^{-14} m^2/s) for basaltic samples. This difference is assigned to the strong tendency of basalt to form secondary minerals during weathering, which shifts the pore size distribution to smaller diameters and increases the tortuosity. In addition, the presence of bound H$_2$O layers, having a thickness of ~ 1.3 nm (Marry et al. 2008) and slowing down self diffusion of water in comparison to bulk water increases the apparent volume of the clay platelets to some extent. The presence of swelling clay minerals such as smectites in samples containing intercalated water, would also slow down the overall self diffusion of the water compared to bulk water (Bourg and Sposito 2011).

Finally clear evidence was obtained that basaltic rocks have a stronger dependence on rock porosity compared to granitic rocks, indicating that specific rock properties significantly influences solute transport and pore solution chemistry. For the porous basalts, pore size seems to be an additional important factor affecting the diffusivity of solutes, i.e., decreasing pore sizes reduces the diffusivity values.

Conclusions

In order to characterize transport in two heterogeneous porous rocks with strong differences in texture and content of secondary minerals, first an extensive characterization of the pores was carried out. Pore space characteristics were determined with three experimental approaches. Well-connected pore spaces with complex pore structures were observed, the pore morphology highly depending on rock type and alteration degrees. From main directions of pores determined in the 3-D-space by X-ray tomography, a slight anisotropy of diffusive transport can be inferred. The use of different filters and image processing operators in the 2-D-space can significantly influence the voxel distribution especially for very small pores. For nm-sized pore diameter advanced techniques such as focused ion beam plus high resolution SEM are needed. Assuming that the pore system is stable at these conditions, this would provide a better data base for geometrical calculations and the use of models to calculate the effect on diffusion.

Wood's metal intrusion offers the possibility for a detailed microscopic characterization of pore morphology and is useful for the critical evaluation of data obtained from Hg-porosimetry, e.g., by detecting pores related to fractures and issues for uneven distribution of pore size.

As the relation between D_{eff} and ϕ was found to be weak for both rocks, different additional factors such as tortuosity, uniformity of pore space characteristics, mineralogical composition of secondary minerals, formation of bound H$_2$O layers, and total and connected porosity have to be considered for ameliorating the prediction of D_{eff}.

Chemical weathering, which can be traced by dissolution/precipitation phenomena within whole rock fragments tends in early stages of weathering to increase porosity and SSA, which induces that the weathering rate can keep stable or is even enhanced. Due to dissolution processes, the connected porosity and the diameter of pores might increase and promote further dissolution reactions. The investigated granitic samples contain only moderate amounts of secondary minerals, but for basaltic samples they can impair further weathering by the extension of the diffusion paths and the covering of surfaces. The detailed knowledge of weathering processes from the fresh to the highly altered rocks including changes in mineralogical composition, porosity and D_{eff} can ameliorate the prognosis of the present function in element turnover of rocks as well as from future states. Here, different processes together with their dependencies can be explained. In

further investigations, the relationship between transport in pore systems and dissolution kinetics has to be examined experimentally.

References

Becker MW, Coplen TB (2001) Use of deuterated water as a conservative artificial groundwater tracer. Hydrogeol J 9:512–516

Behrens H (1995) Determination of water solubilities in high-viscosity melts: and experimental study on $NaAlSi_3O_8$ and $KAlSi_3O_8$ melts. Eur J Mineral 7:905–920

Benning JL, Barnes DL (2009) Comparison of modeling methods for the determination of effective porosities and diffusion coefficients in through-diffusion tests. Water Resour Res 45:W09419. doi:10.1029/2008WR007236

Bourg I, Sposito G (2011) Molecular dynamics simulations of the electrical double layer on smectite surfaces contacting concentrated mixed electrolyte ($NaCl–CaCl_2$) solutions. J Colloid Interf Sci 360:701–715

Bourg IC, Sposito G, Bourg ACM (2006) Tracer diffusion in compacted, water-saturated bentonite. Clays Clay Mineral 54:363–374

Bradbury MH, Green A (1985) Measurement of important parameters determining aqueous phase diffusion rates through crystalline rock matrices. J Hydrol 82:39–55

Brantley SL, Mellott NP (2000) Surface area and porosity of primary silicate minerals. Am Mineral 85:1767–1783

Brunauer S, Emmett PH, Teller E (1938) Adsorption of gases in multimolecular layers. J Am Chem Soc 60:309–319

Cormenzana JL, Garcia-Gutierrez M, Missana T, Junghanns A (2003) Simultaneous estimation of effective and apparent diffusion coefficient in compacted bentonite. J Contam Hydrol 61:63–72

Cussler EL (1997) Diffusion—mass transfer in fluid systems, 2nd edn. Cambridge University Press, Cambridge, p 581

Darot M, Reuschle T (2003) Wood's metal dynamic wettability on quartz, granite, and limestone. Pure Appl Geophys 160:1415–1427

Dullien FAL (1992) Porous media fluid transport and pore structure. Academic Press, San Diego

Dultz S, Behrens H, Simonyan A, Kahr G, Rath T (2006) Determination of porosity and pore connectivity in feldspars from soils of granite and saprolite. Soil Sci 171:675–694

Ganyaglo SY, Banoeng-Yakubo B, Osae S, Dampare SB, Fianko JR (2011) Water quality assessment of groundwater in some rock types in parts of the eastern region of Ghana. Environ Earth Sci 62:1055–1069

Garcia-Gutierrez M, Guimera J, Yllera de Llano A, Hernandez Bentitez A, Humm J, Saltink M (1997) Tracer test at El Berrocal site. J Contam Hydrol 26:179–188

Grathwohl P (1998) Diffusion in natural porous media: contaminant transport, sorption/desorption and dissolution kinetics. Kluwer, Boston, p 2007

Hildenbrand A, Urai JL (2003) Investigation of the morphology of pore space in mudstones—first results. Marine Petrol Geol 20:1185–1200

Himmelsbacher T, Hoetzl H, Maloszewski P (1998) Solute transport processes in a highly permeable fault zone of Lindau fractured rock test site (Germany). Groundwater 36:792–800

Hölttä P, Poteri A, Siitari-Kauppi M, Huittinen N (2008) Retardation of mobile radionuclides in granitic rock fractures by matrix diffusion. Phys Chem Earth 33:983–990

Hu Q, Ewing RP, Dultz S (2012) Low pore connectivity in natural rock. J Contam Hydrol 133:76–83

Huesman RH, Gullberg GT, Greenberg WL, Budinger TF (1977) Report Pub 214. Lawrence Berkeley Laboratory, University of California

Huysmans M, Dassargues A (2012) The effect of heterogeneity of diffusion parameters on chloride transport in low-permeability argillites. Environ Earth Sci. doi:10.1007/s12665-012-1871-0

Jakob A, Mazurek M, Heer W (2003) Solute transport in crystalline rocks at ÄspöII: blind predictions, inverse modelling and lessons learnt from test STT1. J Contam Hydrol 61:175–190

Kaestner A, Schneebeli M, Graf F (2006) Visualizing three-dimensional root networks using computed tomography. Geoderma 136:459–469

Kalman D (1996) A singularly valuable decomposition: the SVD of a matrix. College Math J 27:2–23

Kaufmann J (2009) Characterization of pore space of cement-based materials by combined mercury and Wood's Metal intrusion. J Am Ceram Soc 92:209–216

Keller LM, Holzer L, Wepf R, Gasser P (2011) 3D geometry and topology of pore pathways in Opalinus clay: implications for mass transport. Appl Clay Sci 52:85–95

Kita H, Iwai T, Nakashima S (1989) Diffusion coefficient measurement of an ion in pore water of granite and tuff. J Jpn Soc Eng Geol 30:84–90

Kozaki T, Inada K, Sato S, Ohashi H (2001) Diffusion mechanism of chloride ions in sodium montmorillonite. J Contam Hydrol 47:159–170

Lee MR, Hodson ME, Parsons I (1998) The role of intergranular microtextures and microstructures in chemical and mechanical weathering: direct comparisons of experimentally and naturally weathered alkali feldspars. Geochim Cosmochim Ac 62:2771–2788

Lever DA, Bradbury MH (1985) Rock matrix diffusion and its implications for radionuclide migration. Mineral Mag 49:245–254

Lever DA, Bradbury MH, Hemingway SJ (1985) The effect of dead-end porosity on rock-matrix diffusion. J Hydrol 80:45–76

Li Y-H, Gregory S (1974) Diffusion of ions in sea water and in deep-sea sediments. Geochim Cosmochim Acta 38:703–714

Lloyd RR, Provis JL, Smeaton KJ, van Deventer JSJ (2009) Spatial distribution of pores in fly ash-based inorganic polymer gels visualised by Wood's metal intrusion. Microporous Mesoporous Mater 126:32–39

Löfgren M (2004) Diffusive properties of granitic rock as measured by in-situ electrical methods. PhD thesis, Department of Chemical Engineering and Technology, Royal Institute of Technology, Stockholm, Sweden, p 85

Lüttge A (2005) Etch pit coalescence, surface area, and overall mineral dissolution rates. Am Mineral 90:1776–1783

Marry V, Rotenberg B, Turq P (2008) Structure and dynamics of water at a clay surface from molecular dynamics simulation. Phys Chem Chem Phys 10:4802–4813

Masaphy S, Zabari L, Pastrana J, Dultz S (2009) Role of fungal mycelium in the formation of carbonate concretions in growing media—an investigation by SEM and synchrotron-based X-ray tomographic microscopy. Geomicrobiol J 26:442–450

Molina Ballesteros E, García Talegón J, Iñigo Iñigo AC, González Sánchez M, Herrero Fernández H (2011) Importance of porosity

and transfer of matter in the rock weathering processes: two examples in central Spain. Environ Earth Sci 64:1741–1754

Navarre-Sitchler A, Steefel CI, Yang L, Tomutsa L, Brantley SL (2009) Evolution of porosity and diffusivity associated with chemical weathering of a basalt clast. J Geophys Res 114 (2):F02016, doi:10.1029/2008JF001060

Park CK, Baik MH (2009) Diffusion of some chemical species through a granite considering their geochemical properties. Korean J Chem Eng 26:1279–1285

Park CK, Park HH (1992) Computer simulation study of transient diffusion of cesium through granite with unsteady-state diffusion model. J Nucl Sci Technol 29:786–793

Peth S, Horn R, Beckmann F, Donath T, Fischer J, Smucker AJM (2008) Three-dimensional quantification of intraaggregate pore space features using synchrotron-radiation-based microtomography. Soil Sci Soc Am J 72:897–907

PODP (1996) Proceedings of the ocean drilling program

Putnis A (2002) Mineral replacement reactions: from macroscopic observations to microscopic mechanisms. Mineral Mag 66:689–708

Sato H (1999) Matrix diffusion of simple cations, anions, and neutral species in fractured crystalline rocks. Nucl Technol 127:199–211

Sato H, Shibutani T, Yui M (1997) Experimental and modelling studies on diffusion of Cs, Ni and Sm in granodiorite, basalt and mudstone. J Contam Hydrol 26:119–133

Schampera B, Dultz S (2009) Determination of diffusive transport in HDPy-montmorillonite by H_2O–D_2O exchange using in situ ATR-FTIR spectroscopy. Clay Miner 44:249–266

Schild M, Siegesmund S, Vollbrecht A, Mazurek M (2001) Characterization of granite matrix porosity and pore-space geometry by in situ laboratory methods. Geophys J Int 146:111–125

Schramm B, Devey CW, Gillis KM, Lackschewitz K (2005) Quantitative assessment of chemical and mineralogical changes due to progressive low temperature alteration of East Pacific Rise basalts from 0 to 9 Ma. Chem Geol 218:281–313

Simonyan AV, Behrens H, Dultz S (2009) Diffusive transport of water in porous feldspars from granitic saprolites: in situ experiments using FTIR spectroscopy. Geochim Cosmochim Acta 73:7019–7033

Simonyan AV, Dultz S, Behrens H (2012) Diffusive transport of water in porous fresh to altered mid-ocean ridge basalts. Chem Geol 306–307:63–77

Thermo Finnigan (2002) Pascal software for pascal porosimeters operating manual, 2nd edn. Thermo Finnigan, Italy, p 136

Vilks P, Cramer JJ, Jensen M, Miller NH, Miller HG, Stanchell FW (2003) In situ diffusion experiment in granite: phase I. J Contam Hydrol 61:191–202

Washburn EW (1921) Note on a method of determining the distribution of pore sizes in a porous material. Proc Natl Acad Sci 7:115–116

Whitney DL, Evans BW (2010) Abbreviations for names of rock-forming minerals. Am Mineral 95:185–187

Widestrand H, Byegård J, Cvetkovic V, Tullborg E-L, Winberg A, Andersson P, Siitari-Kauppi M (2007) Sorbing tracer experiments in a crystalline rock fracture at Äspö (Sweden): 1. Experimental setup and microscale characterization of retention properties. Water Resour Res 43:W10413. doi:10.1029/2006 WR005277

Wilson MJ (2004) Weathering of the primary rock-forming minerals: processes, products and rates. Clay Miner 39:233–266

Xu S, Wörman A, Dverstorp B (2001) Heterogeneous matrix diffusion in crystalline rock—implications for geosphere retardation of migrating radionuclides. J Contam Hydrol 47:365–378

Zhou Q, Liu H–H, Bodvarsson GS, Molz FJ (2006) Evidence of multi-process matrix diffusion in a single fracture from a field tracer test. Transpod Porous Media 63:473–487